water

MDPI

Article

Hydraulic Coupling-Induced Flow-Regime Transition and Energy Dissipation Characteristics in Cascade Flood Discharge Systems of Large Tailings Storage Facilities

Hongbo Xia [1], Xinyi Li [2], Shaoxiong Zhang [2,*], Sa Yang [2], Zhenyuan Cheng [2] and Yuhao Bao [2]

[1] Information Institute of the Ministry of Emergency Management, Beijing 100029, China; xiahb@iiem.ac.cn
[2] School of Civil Engineering, Shijiazhuang Tiedao University, Shijiazhuang 050043, China; audreyli72777@163.com (X.L.); yangsa022519@163.com (S.Y.); chengzhenyuan22@outlook.com (Z.C.); 18331037574@163.com (Y.B.)
* Correspondence: zhangsx@stdu.edu.cn

Abstract

Hydraulic analysis of complex flood-drainage systems is critical for the safety design of large tailings storage facilities. Conventional approaches are limited in their ability to precisely characterize three-dimensional flow fields and flow-regime transition processes under multi-structure coupling conditions. A three-dimensional FLOW-3D model was developed for the Diyan tailings storage facility using the RNG k-ε turbulence model and Tru-VOF method. The system comprises three internal drainage shafts, three external overflow shafts, and more than 4 km of connecting tunnels. Simulated discharges exceeded the corresponding design values by 2.3–26.5%. All internal drainage tunnels remained under free-surface flow. The available CFD cases bracketed the free-surface–pressurized transition of the coupled No. 1 and No. 2 overflow shafts between upstream heads of 1.0 and 2.0 m. Downstream hydraulic control propagated backwater through the connecting tunnels, altered the upstream flow regime, and reduced the rate of discharge increase. Total-head dissipation ratios ranged from 58.2% to 99.7%. Within the internal drainage system, larger vertical drops were generally associated with lower residual outlet velocities and higher dissipation ratios. The results provide an engineering-scale numerical assessment of hydraulic interaction, backwater propagation, and flow-regime change in a cascade flood discharge systemfor the hydraulic evaluation of similar configurations.

Keywords: tailings storage facility; cascade flood discharge system; FLOW-3D; flow-regime transitions; energy dissipation

Check for updates

Academic Editor: Bommanna Krishnappan

Received: 31 August 2026
Revised: 10 September 2026
Accepted: 22 September 2026
Published: 25 September 2026

Copyright: © 2026 by the authors. Licensee MDPI, Basel, Switzerland. This article is an open access article distributed under the terms and conditions of the Creative Commons Attribution (CC BY) license.

1. Introduction

The flood discharge safety of large tailings storage facilities depends on whether the drainage system can maintain sufficient conveyance capacity during flood events. Tailings dam failures have caused severe casualties, economic losses, and environmental damage worldwide [1]. Flood overtopping during extreme rainfall is also recognized as an important failure trigger [2–4]. Rana [5] reviewed global tailings-flow events from 1928 to 2020, showing that such failures remain a persistent safety concern. Numerical modelling has increasingly been used to examine dam breach, runout, and related uncertainties [6]. Flood inflow is not controlled by rainfall alone. Catchment conditions and hydrological variability can also affect runoff response [7,8], which makes the hydraulic performance of

large tailings discharge systems under changing inflow conditions an important engineering issue.

Large tailings discharge systems usually contain several drainage shafts, long conveyance tunnels, and energy dissipation structures. Their hydraulic behaviour is therefore more complicated than that of an isolated shaft. Liu et al. [9] studied the discharge capacity of a flood discharge shaft in a tailings reservoir, Zhang et al. [10] examined the hydraulic characteristics of a vortex drop shaft, and Crispino et al. [11] investigated energy dissipation and pressure distributions in vortex drop shafts. Zhang et al. [12] further analyzed a complex tailings spillway system under extreme weather conditions. These studies provide a useful basis for understanding individual structures and local flow processes. Physical models can directly show water-surface and flow-regime changes, while validated CFD can provide detailed velocity, pressure, and free-surface information [9,13]. Once several shafts share the same downstream tunnel, however, they no longer behave as fully independent hydraulic units.

Free-surface–pressurized flow transition has been widely studied in tailrace tunnels, water-conveyance tunnels, and deep drainage systems. Zhou and Li [14] developed a unified model for mixed free-surface and pressurized flow. Huang et al. [15] studied interface capture in large cascade water-delivery systems, while Wang et al. [16] examined tunnel filling with entrapped air in a two-shaft–one-tunnel system. Zhang et al. [17,18] further investigated flow-regime transition and water–air interaction under different tunnel and inflow conditions. These studies have clarified many aspects of mixed flow, air entrapment, and transient pressure behaviour. Less attention has been given to the hydraulic interaction among multiple flood discharge shafts connected by long tunnels. A key issue remains unresolved: when downstream conveyance becomes restricted, how far the resulting backwater extends upstream and how it changes the hydraulic state of upstream shafts.

This study investigates the multi-stage cascade flood discharge system of the Diyan tailings storage facility using a three-dimensional FLOW-3D model with the RNG k-ε turbulence model and the Tru-VOF method. The model includes three internal drainage shafts, three external overflow shafts, and more than 4 km of connecting tunnels. The analysis focuses on three questions: how hydraulic coupling affects the discharge behaviour and available margins of individual structures; how downstream backwater influences the transition from free-surface to pressurized flow; and how residual outlet velocity and total-head dissipation differ among the investigated shaft configurations. Local high-velocity regions near shaft bottoms and energy dissipation zones are also examined to identify locations with relatively high hydraulic loading.

2. Materials and Methods

2.1. Engineering Background

The Diyan tailings storage facility is located in a valley southeast of the Diyan processing plant in China, with a total dam height of 83 m, a storage capacity of 2.70×10^8 m^3, and a catchment area of 15.71 km^2. Classified as a Class II tailings storage facility, it adopts an upstream construction scheme. The flood discharge system comprises an internal drainage subsystem and an external overflow subsystem, with interconnected tunnels exceeding 4 km in total length (Figure 1).

The internal drainage subsystem includes three drainage shafts, branch tunnels, and a main tunnel, with a total length of approximately 1.8 km. The No. 0 drainage shaft has a diameter of 3 m and a height of 9 m, and connects to the main tunnel through a 474 m branch tunnel (2.0 m × 2.0 m, slope 1.5%). The No. 1 drainage shaft has a diameter of 4 m and a height of 30 m, connected through a 162 m branch tunnel (2.6 m × 2.6 m, slope 2.0%). The No. 2 drainage shaft has a diameter of 4 m and a height of 30 m and is connected to the

main tunnel through a 35.5 m vertical shaft with a diameter of 3.5 m. The main tunnel is 1164 m long, with a cross-section of 2.6 m × 2.6 m and a slope of 2.0%. A stilling basin is installed at the tunnel outlet.

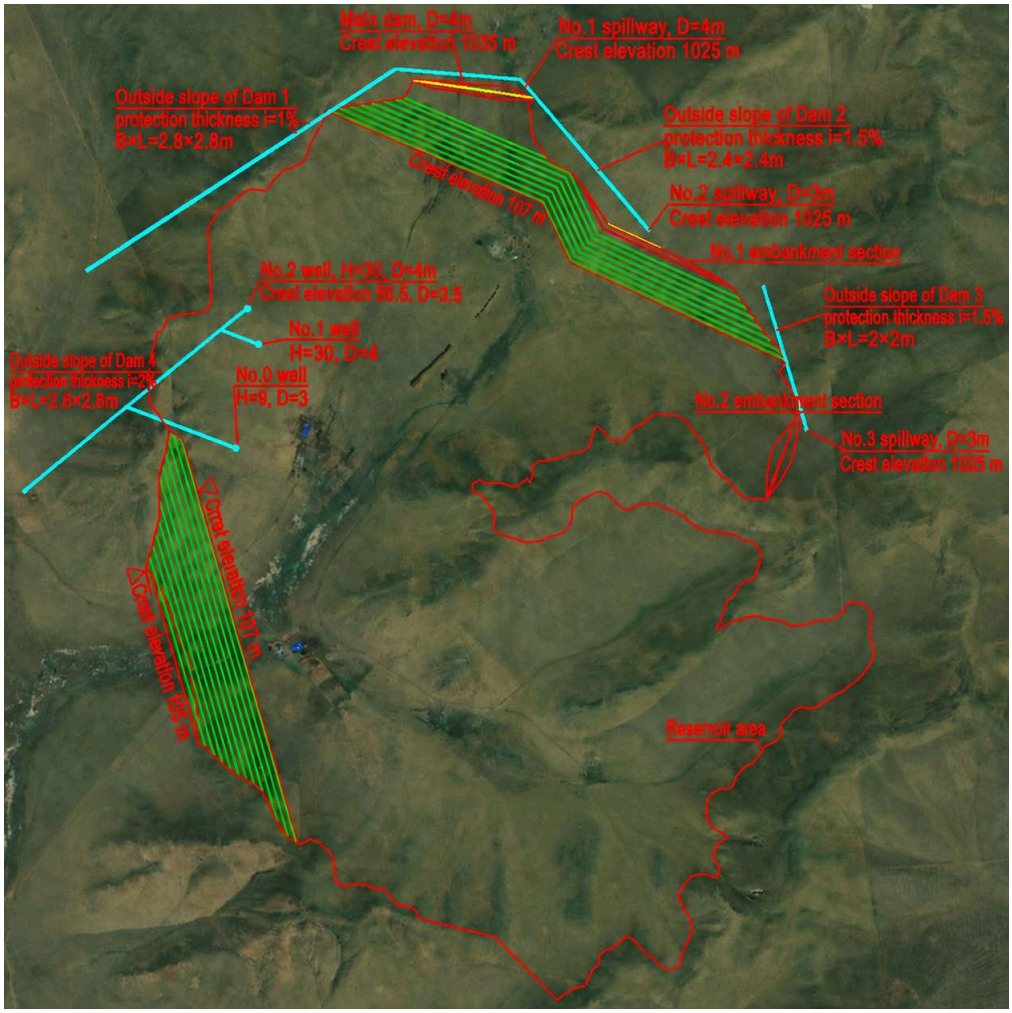


Figure 1. Layout of the internal drainage and external overflow systems of the Diyan tailings storage facility.

The external overflow subsystem comprises a hydraulically coupled No. 1–No. 2 overflow system and an independent No. 3 overflow system, with a total tunnel length of approximately 3.4 km. The No. 1 overflow shaft has a diameter of 4 m and a height of 19 m and is followed by a 2000 m tunnel with a cross-section of 2.8 m × 2.8 m and a slope of 1.0%. The No. 2 overflow shaft has a diameter of 3 m and a height of 6.5 m. Its discharge enters the No. 1 system through an 800 m tunnel with a cross-section of 2.4 m × 2.4 m and a slope of 1.5%. The No. 3 overflow shaft has a diameter of 3 m and a height of 5.7 m and discharges independently through a 600 m tunnel with a cross-section of 2.0 m × 2.0 m and a slope of 1.5%. The flood routing follows the overflow shaft sequence of No. 3 → No. 2 → No. 1. All tunnel sections are of an arched-rectangular cross-section with 0.3 m thick C30 reinforced concrete permanent lining and 0.1 m thick C20 shotcrete temporary support during construction.

2.2. Numerical Model and Methods

2.2.1. Governing Equations, Numerical Methods, and Hydraulic Evaluation

The governing equations were solved using the FLOW-3D, version 11.2, Flow Science, Inc., Santa Fe, NM, USA. The mass conservation equation was formulated in volume-

fraction form to account for irregular geometric boundaries. For incompressible flow, the continuity equation is expressed as

$$\frac{\partial}{\partial x}(uA_x)+\frac{\partial}{\partial y}(vA_y)+\frac{\partial}{\partial z}(wA_z)=0 \quad (1)$$

where u, v, and w are the velocity components in the x-, y-, and z-directions, respectively, and Ax, Ay, and Az are the corresponding fluid area fractions [19].

Momentum conservation equations were solved in the three coordinate directions. The general form of the x-direction equation is expressed as

$$\frac{\partial u}{\partial t}+\frac{1}{V_F}\{uA_x\frac{\partial u}{\partial x}+vA_y\frac{\partial u}{\partial y}+wA_z\frac{\partial u}{\partial z}\}=-\frac{1}{\rho}\frac{\partial p}{\partial x}+G_x+f_x \quad (2)$$

where V_F is the fluid volume fraction, ρ is the fluid density, p is the pressure, G_x is the gravitational acceleration component, and f_x represents the viscous acceleration term. Wall functions were applied to account for near-wall shear effects.

The Reynolds-averaged Navier–Stokes (RANS) equations were closed using the RNG k-ε turbulence model [20]. The conventional k–ε framework has been widely used for engineering turbulent-flow calculations [21], while the RNG formulation introduces modifications derived from renormalization-group theory and is better suited to flows involving strong strain, curvature, and separation. These characteristics are relevant to the present flood discharge system, particularly near shaft inlets, vertical drops, and shaft-bottom dissipation regions.

The transport equation for turbulent kinetic energy k is

$$\frac{\partial}{\partial t}(\rho k)+\frac{\partial}{\partial x_j}(\rho U_j k)=\frac{\partial}{\partial x_j}(\frac{\mu_e}{\sigma_k}\frac{\partial k}{\partial x_j})+P_k+P_b-\rho\varepsilon \quad (3)$$

The transport equation for the turbulent dissipation rate ε is

$$\frac{\partial}{\partial t}(\rho\varepsilon)+\frac{\partial}{\partial x_k}(\rho U_k\varepsilon)=\frac{\partial}{\partial x_k}(\frac{\mu_e}{\sigma_e}\frac{\partial\varepsilon}{\partial x_k})+\frac{\varepsilon}{k}(c_{\varepsilon1}P_k-\rho c_{\varepsilon2}\varepsilon)+c_{\varepsilon3}\frac{\varepsilon}{k}P_b \quad (4)$$

where k is the turbulent kinetic energy, ε is its dissipation rate, U_j and U_k are the time-averaged velocity components, x_j and x_k are the spatial coordinates, μ_e is the effective viscosity, σ_k and σ_ε are the turbulent Prandtl numbers for k and ε, respectively, P_k is the production term of turbulent kinetic energy, and P_b represents turbulent kinetic energy production due to buoyancy. The model constants $c_{\varepsilon1}$, $c_{\varepsilon2}$, and $c_{\varepsilon3}$ were set to 1.45, 1.91, and 1.17, respectively [19,20].

The turbulent viscosity is expressed as

$$v_t=C_\mu\frac{k^2}{\varepsilon} \quad (5)$$

where Cμ is set to 0.09. The remaining model parameters were assigned the default values implemented in FLOW-3D [19,20].

The free-surface evolution was captured using the Tru-VOF method implemented in FLOW-3D [19]. The method is based on the Volume of Fluid (VOF) approach proposed by Hirt and Nichols [22], where a fluid volume fraction F = 0 denotes an empty cell, 0 < F < 1 indicates the presence of a free surface, and F = 1 represents a cell completely filled with fluid. The governing equation for F is

$$\frac{\partial F}{\partial t}+\frac{1}{V_F}(uA_x\frac{\partial F}{\partial x}+vA_y\frac{\partial F}{\partial y}+wA_z\frac{\partial F}{\partial z})=0 \quad (6)$$

Unlike conventional VOF approaches, Tru-VOF mainly solves cells containing fluid, improving computational efficiency [19].

The governing equations were discretized using a finite-difference scheme on a structured staggered grid. Pressure and density were stored at cell centres, whereas velocity components were defined at cell faces [19,23].

Total-head dissipation was evaluated between the shaft inlet and the downstream tunnel outlet, with the tunnel-outlet invert taken as the elevation datum. The total head was defined as

$$E = H + \frac{p}{\gamma} + \frac{v^2}{2g} \tag{7}$$

where H, p/γ, and $v^2/2g$ are the elevation, pressure, and velocity heads, respectively. The dissipation ratio was calculated as

$$\eta = \frac{E_1 - E_2}{E_1} \tag{8}$$

where E_1 and E_2 are the total heads at the shaft inlet and tunnel outlet.

2.2.2. Computational Domain and Mesh Generation

A three-dimensional computational model of the flood discharge systems was developed based on engineering design drawings (Figure 2). The model included both the internal drainage and external overflow subsystems, with shaft and tunnel geometries reproduced according to the prototype structures. The external subsystem comprised a hydraulically coupled No. 1–No. 2 overflow system and an independent No. 3 overflow system, while the internal subsystem included three independently operated drainage-shaft systems.

A consistent meshing strategy was applied to all computational domains. A multi-block structured Cartesian mesh was adopted in FLOW-3D [19], with the external No. 1–No. 2 overflow system divided into 44 mesh blocks. Local refinement was applied near the shaft inlets, shaft–tunnel junctions, and other regions characterized by pronounced streamline curvature, free-surface deformation, and local velocity gradients. In the production mesh, a cell size of 0.05 m × 0.05 m × 0.05 m was used in these locally refined regions, whereas 0.20 m × 0.20 m × 0.20 m cells were adopted in the relatively uniform tunnel reaches.

The mesh resolution was selected with reference to the characteristic dimensions of the hydraulic structures. Approximately six cells were used to resolve the gaps between the drainage-shaft columns, while 10–14 cells were distributed across the transverse and vertical directions of the tunnel sections to represent the free-surface profile and cross-sectional flow structure.

A three-level mesh convergence assessment was performed using coarse, medium, and fine meshes. Cell sizes in the locally refined regions/general tunnel reaches were 0.10/0.40 m, 0.05/0.20 m, and 0.025/0.10 m, respectively, giving a constant refinement ratio of r = 2. The medium mesh was used as the production mesh. Geometry, RNG k-ε turbulence model, Tru-VOF treatment, boundary conditions, and wall roughness were kept unchanged among the three cases.

Mesh effects were examined under two representative conditions. For the coupled No. 1–No. 2 external overflow system, the discharges Q_1 and Q_2 were monitored. For the internal No. 2 drainage shaft at the design head, the stabilized tunnel flow depth h and cross-sectional mean velocity V were compared.

Grid convergence was quantified using Richardson extrapolation. With ϕ_1, ϕ_2 and ϕ_3 denoting the fine-, medium-, and coarse-mesh solutions, respectively, the apparent order of convergence was calculated as

$$p = \frac{ln\left|\frac{\phi_3-\phi_2}{\phi_2-\phi_1}\right|}{lnr} \tag{9}$$

The Grid Convergence Index (GCI) was evaluated using a safety factor of 1.25:

$$GCI_{21} = \frac{1.25}{r^p-1}\left|\frac{\phi_1-\phi_2}{\phi_1}\right| \times 100\% \tag{10}$$

$$GCI_{32} = \frac{1.25}{r^p-1}\left|\frac{\phi_2-\phi_3}{\phi_2}\right| \times 100\% \tag{11}$$

Table 1 summarizes the response of the four monitored quantities to mesh refinement. All four showed monotonic convergence, with an apparent convergence order of approximately 2.0. The fine-grid GCI ranged from 0.084% to 0.143%, while the medium-to-fine differences remained between 0.20% and 0.34%. The asymptotic convergence ratios were close to unity. The medium mesh was retained for the subsequent simulations, as further refinement changed the monitored hydraulic quantities only slightly while substantially increasing the computational demand of the long tunnel domains.

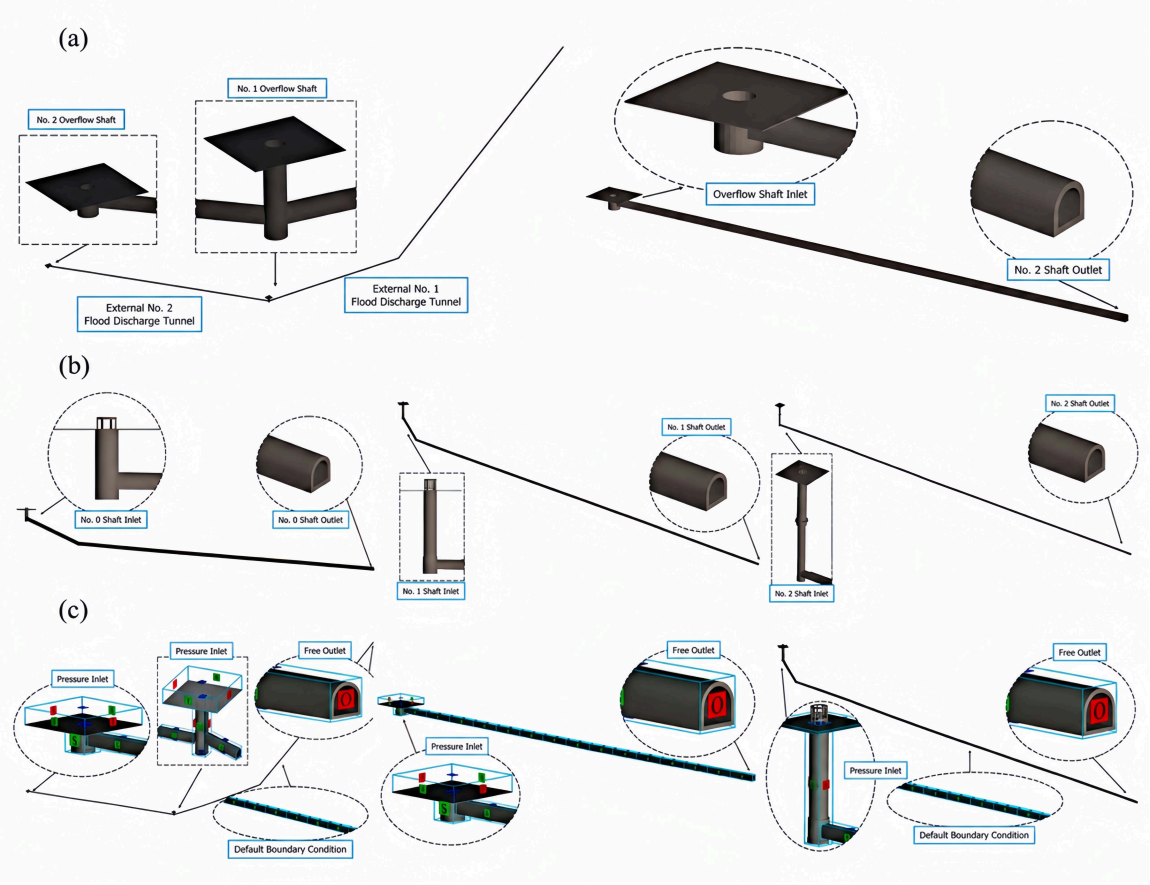


Figure 2. Three-dimensional geometry models, computational meshes, and boundary conditions of the flood discharge systems: (**a**) external overflow shaft systems; (**b**) internal drainage-shaft systems; and (**c**) computational meshes and boundary conditions.

The boundary conditions were defined according to the hydraulic conditions of the prototype system. A prescribed pressure head corresponding to the upstream water level was imposed at the shaft inlets, while a free-outflow condition was applied at the tunnel outlets. The concrete-lined shaft and tunnel walls were assigned a roughness coefficient of

0.014. The simulations were considered quasi-steady when the discharge variation between successive iterations was less than 0.5%.Each prescribed-head condition was simulated independently and interpreted as a quasi-steady hydraulic state rather than a transient filling process.

Table 1. Three-level mesh convergence and Grid Convergence Index assessment for representative hydraulic quantities.

Variable	Coarse	Medium	Fine	Medium–Fine Difference (%)	p	GCI_{21}(%)	GCI_{32} (%)	Asymptotic Ratio
External No. 1 Q_1 (m^3/s)	44.440	44.800	44.890	0.200	2.00	0.084	0.335	1.002
External No. 2 Q_2 (m^3/s)	33.020	33.300	33.370	0.210	2.00	0.087	0.350	1.002
Internal No. 2 h(m)	0.286	0.290	0.291	0.344	2.00	0.143	0.575	1.003
Internal No. 2 V (m/s)	3.510	3.550	3.560	0.281	2.00	0.117	0.469	1.003

2.3. Simulation Cases

Simulation cases were designed to evaluate the hydraulic performance of the discharge system under different operating conditions. The prescribed upstream heads were selected according to the flood-control requirements specified in the Code for Design of Tailings Facilities [24] and the Safety Regulations for Tailings Ponds [25]. The internal subsystem included the No. 0, No. 1, and No. 2 drainage shafts, whereas the external subsystem included the No. 1–No. 3 overflow shafts. The applicable flood return period varies with the operating stage and classification of the tailings storage facility. The prescribed heads and corresponding simulation cases are summarized in Table 2.

Table 2. Summary of simulation cases.

System	Structure	Head Over the Crest, H (m)	No. of Cases
Internal	No. 0 drainage shaft	0.40, 0.60, 0.85, 1.31 *	4
Internal	No. 1 drainage shaft	0.12, 0.24, 0.36, 0.43 *	4
Internal	No. 2 drainage shaft	0.08, 0.12, 0.17, 0.27 *	4
External	No. 1 overflow shaft	1.0, 2.0, 3.0, 4.0, 6.29 *	5
External	No. 2 overflow shaft	1.0, 2.0, 3.0, 4.0, 5.28 *	5
External	No. 3 overflow shaft	0.5, 1.0, 1.5, 2.0, 2.63 *	5

Note: An asterisk indicates the design-flood head corresponding to the operating stage of each structure. The No. 1 and No. 2 overflow shafts operate jointly, whereas the internal drainage shafts operate independently. The crest elevations of the No. 1 and No. 2 overflow shafts are both 1025.0 m. Their design-flood heads of 6.29 m and 5.28 m correspond to the respective maximum flood levels obtained from the flood-routing calculations for their upstream impoundment areas.

2.4. Hydraulic Consistency and Roughness-Sensitivity Assessment

The mesh sensitivity analysis described above was used to check whether the numerical solution changed appreciably with spatial resolution. It did not, however, provide an independent check of the hydraulic reasonableness of the model results. Direct field measurements or dedicated physical-model data were not available for the present cascade system, so a formal experimental validation was not feasible. A simpler engineering-scale check was therefore used before the simulated results were interpreted further. This is not validation in the strict sense, but it provides a practical way to assess whether the computed

hydraulic response is consistent with the available design information and with the general verification practice discussed in the CFD literature [26,27].

At the system scale, the simulated discharges under the design-flood conditions were compared with the corresponding hydraulic design values, as reported later in Section 3.1. These values provide a practical reference for the overall discharge level of each structure. A second check was carried out for the internal drainage tunnels, where the simulated water-surface profiles showed that the flow became nearly uniform after the local adjustment downstream of the shaft and tunnel transitions.

The Manning equation was used to estimate the normal-flow condition in these stabilized free-surface reaches [28]

$$Q = \frac{1}{n} A R^{\frac{2}{3}} S^{\frac{1}{2}} \tag{12}$$

with

$$R = \frac{A}{P} \tag{13}$$

where Q is the discharge, n is the Manning roughness coefficient, A is the wetted area, R is the hydraulic radius, P is the wetted perimeter, and S is the tunnel bed slope. A Manning roughness coefficient of n = 0.014 was adopted for the analytical uniform-flow calculation. For the selected shallow-flow cases, the wetted section was represented by the straight-wall part of the tunnel section, giving $A = B_y$ and $P = B + 2y$.

The comparison was restricted to the No. 1 and No. 2 internal drainage systems. Their downstream reaches exhibited nearly constant flow depths over several consecutive sections, whereas the No. 0 system showed a more pronounced water-surface adjustment after the branch tunnel entered the main tunnel. Both selected reaches had a width of 2.6 m and a bed slope of 2.0%. The CFD discharge was introduced into Equation (12), and the corresponding Manning normal depth yM was obtained iteratively. The comparison results are summarized in Table 3.

Table 3. Hydraulic consistency between CFD results and Manning uniform-flow calculations.

Structure	B (m)	S	Q_{CFD} (m^3/s)	y_{CFD} (m)	y_M (m)	v_{CFD} (m/s)	vM (m/s)	δ_y (%)
No. 1 drainage shaft	2.6	0.020	6.07	0.47	0.470	4.97	4.97	0.05
No. 2 drainage shaft	2.6	0.020	2.68	0.29	0.275	3.55	3.76	5.65

The relative difference in water depth was calculated as

$$\delta_y = \frac{|y_{CFD} - y_M|}{y_M} \times 100\% \tag{14}$$

For the No. 1 system, the Manning depth was 0.470 m, almost identical to the CFD value of 0.47 m, and the velocities matched equally well. The No. 2 system showed a somewhat larger discrepancy: the calculated normal depth was 0.275 m against a CFD depth of 0.29 m, giving a relative difference of 5.65%, with corresponding velocities of 3.76 and 3.55 m/s. The comparison indicates that the simulated conveyance behaviour in these two stabilized free-surface reaches is broadly consistent with the Manning calculation. This agreement is used only as a hydraulic consistency check for the selected reaches and should not be interpreted as validation of the more complex flow conditions elsewhere in the system.

The Manning comparison was not extended to the coupled No. 1–No. 2 external overflow system. As the upstream head increases, backwater develops and parts of the downstream tunnel approach or enter pressurized flow. The assumptions of steady, uniform

open-channel flow no longer apply under these conditions. The hydraulic behaviour of this part of the system was therefore examined from the three-dimensional CFD results rather than by extending the Manning comparison beyond its applicable range.

The roughness coefficient is also relevant to the coupled system because the No. 1–No. 2 overflow shafts are connected by long tunnel reaches. Additional FLOW-3D simulations with alternative roughness values were not performed in the present study. The influence of roughness was therefore examined through a first-order analytical sensitivity assessment rather than additional CFD runs.

For a given discharge and cross-section, the Manning relation gives $S_f \propto n^2$ and the corresponding frictional head-loss ratio can be written as

$$\frac{h_f(n)}{h_f(n_0)} = (\frac{n}{n_0})^2 \quad (15)$$

where hf(n) is the frictional head loss associated with roughness n, n0 is the baseline Manning roughness coefficient, and hf(n0) is the corresponding baseline frictional head loss. The analytical sensitivity results are summarized in Table 4.

Table 4. First-order analytical sensitivity of frictional head loss to Manning roughness.

n	Change from Baseline	$h_f/h_{f,0}$	Change in Frictional Head Loss
0.0112	−20%	0.64	−36%
0.014	0	1.00	0
0.0168	+20%	1.44	+44%

A 20% decrease in the Manning coefficient reduces the estimated frictional head-loss term to about 64% of the baseline value, whereas a 20% increase raises it to about 144%. The calculation shows that the longitudinal friction term in the long tunnel reaches is sensitive to the assumed roughness.

This result should not be read as a direct estimate of how far the free-surface–pressurized transition head would move if the roughness changed. The coupled response also depends on local losses, flow redistribution between shafts, downstream water level, and changes in the free surface. The transition range discussed later in this paper therefore represents the range identified from the available CFD cases for the baseline roughness n = 0.014. It is not treated as a roughness-independent critical head.

3. Results

3.1. Discharge Capacity Characteristics and Hydraulic Constraints

The three internal drainage shafts exhibited independent hydraulic responses under all simulated conditions. Under the design-flood conditions, the simulated discharges of the No. 0, No. 1, and No. 2 drainage shafts were 18.92, 6.07, and 2.68 m^3/s, respectively, corresponding to relative differences of 5.9–26.5% from the design discharges. The H–Q relationships increased nonlinearly with increasing upstream head (Figure 3a–c). At low heads, discharge was mainly controlled by crest overflow, whereas inlet submergence became increasingly influential as the head increased. All connecting tunnels remained under free-surface flow, and no evident downstream restriction was observed within the simulated range.

The external overflow system exhibited different hydraulic behaviour due to the cascade arrangement. The No. 3 overflow shaft operated independently from the downstream coupled section and maintained free-surface flow throughout the simulated range (Figure 3f). Its simulated discharge under the design-flood condition was 20.58 m^3/s, corresponding to a relative difference from the design discharge of 11.4%. In contrast, the

No. 1 and No. 2 overflow shafts formed a coupled hydraulic system, and their H–Q curves showed reduced growth rates with increasing upstream head (Figure 3d,e). The change in discharge response occurred within an upstream head range of 1.0–2.0 m, corresponding to the flow transition interval discussed in Section 3.2. Under the design-flood condition, the simulated discharges of the No. 1 and No. 2 overflow shafts were 44.8 and 33.3 m^3/s, with the relative differences of 2.3% and 8.5%, respectively.

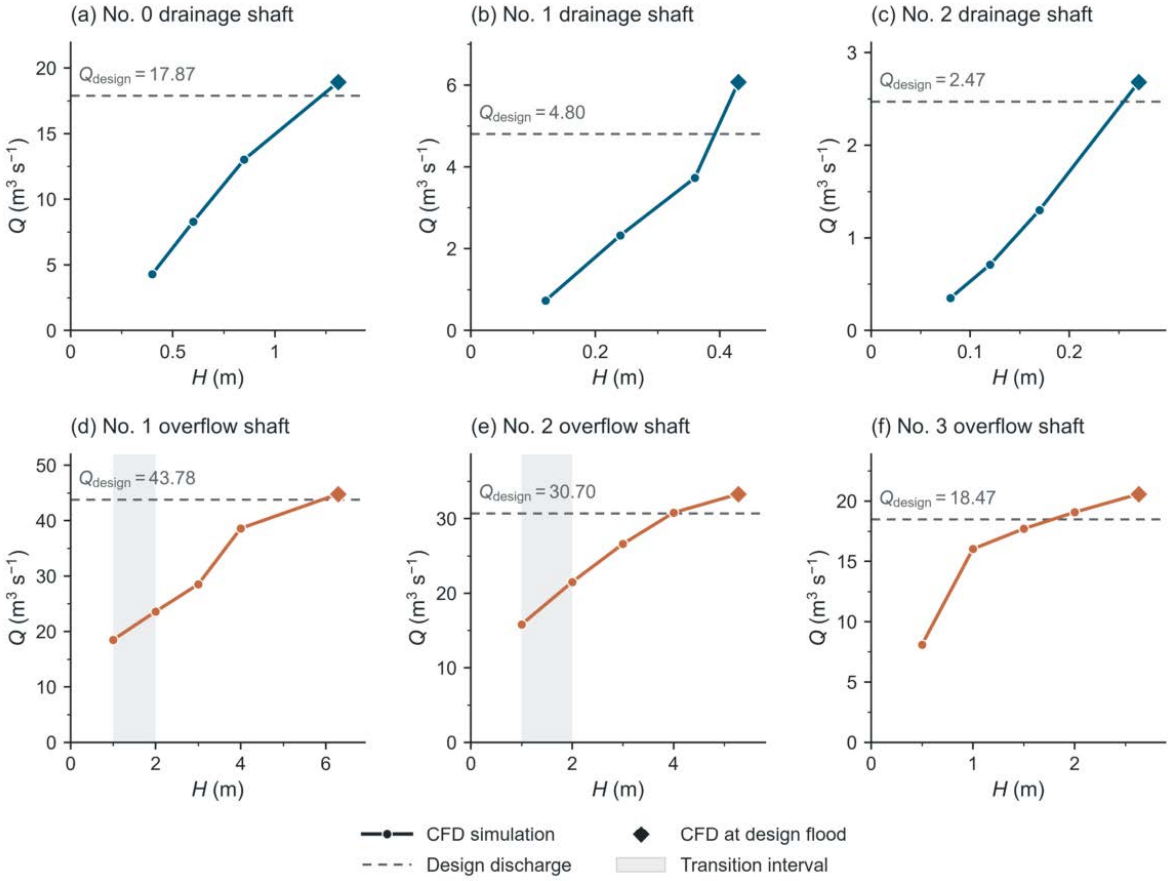


Figure 3. Head–discharge relationships and flow-regime transition intervals of the internal drainage and external overflow shafts under different upstream heads. (**a**) No. 0 drainage shaft; (**b**) No. 1 drainage shaft; (**c**) No. 2 drainage shaft; (**d**) No. 1 overflow shaft; (**e**) No. 2 overflow shaft; and (**f**) No. 3 overflow shaft. Solid lines with circular markers show the CFD-predicted H–Q relationships, horizontal dashed lines indicate the design discharges, and diamond markers denote the CFD results under the design-flood conditions. The shaded regions in (**d**,**e**) indicate the simulated transition interval between free-surface and pressurized flow.

The discharge performance of all six structures is summarized in Table 5. All simulated discharges exceeded the design requirements, with relative difference from the design discharges ranging from 2.3% to 26.5%. For the external overflow system, the relative difference from the design discharge decreased from the independently operating No. 3 overflow shaft to the downstream No. 1 overflow shaft (11.4% → 8.5% → 2.3%). The smallest relative difference occurred for the No. 1 overflow shaft, where the strongest downstream hydraulic constraint was observed. Individual overflow shafts in cascade systems should therefore be evaluated together with the connected conveyance system rather than as isolated structures.

Table 5. Comparison of simulated and design discharges under the design-flood conditions.

System	Structure	(H) at Design Flood (m)	Simulated Discharge (m^3/s)	Design Discharge (m^3/s)	Relative Difference from Design Discharge (%)
Internal	No. 0 drainage shaft	1.31	18.92	17.87	5.9
Internal	No. 1 drainage shaft	0.43	6.07	4.80	26.5
Internal	No. 2 drainage shaft	0.27	2.68	2.47	8.5
External	No. 1 overflow shaft	6.29	44.8	43.78	2.3
External	No. 2 overflow shaft	5.28	33.3	30.70	8.5
External	No. 3 overflow shaft	2.63	20.58	18.47	11.4

Note: The relative difference was calculated as $(Q_{CFD} - Q_{design})/Q_{design} \times 100\%$. It represents the difference between the simulated and engineering design discharges and is not treated as an independently validated safety margin.

3.2. Flow-Regime Evolution and Hydraulic Interaction in the Discharge Systems

3.2.1. Hydraulic Response of the Internal Drainage-Shaft Subsystem

The three internal drainage shafts received lateral inflows through framed inlet structures. The inlet columns divided the incoming flow into multiple water nappes before entering the shafts. No persistent wall-attached flow or obvious vortex structures were observed, and the downstream dissipation process only caused limited water-level variation near the shaft bottoms without affecting upstream inlet conditions.

The longitudinal flow-depth distributions along the connecting tunnels are shown in Figure 4. Under all simulated heads, flow depth varied gradually along the tunnel reaches, with only local changes near structural transitions. Under the design-flood condition, the flow depths downstream of the No. 0, No. 1, and No. 2 drainage shafts were 1.32, 0.47, and 0.29 m, respectively, with corresponding cross-sectional mean velocities of 5.51, 4.97, and 3.55 m/s (Table 6). All calculated flow depths remained below the tunnel heights, indicating that the internal drainage tunnels operated under free-surface conditions.

The longitudinal velocity fields under low-head and design-flood conditions are presented in Figure 5. Velocity distributions remained relatively uniform along the tunnel reaches for all three drainage shafts, without evident local flow acceleration or unstable flow patterns. Although higher upstream heads increased flow velocity, the overall flow pattern remained stable. Together with the flow-depth results, these observations confirm that the internal drainage tunnels maintained free-surface conveyance and were not significantly affected by downstream hydraulic conditions.

Table 6. Characteristic water depth and cross-sectional mean velocity in the internal tunnels under the design-flood conditions.

Structure	Tunnel Cross-Section(m)	Head over the Crest,(H)(m)	Water Depth (m)	Mean Velocity (m/s)	Flow Regime
No. 0 drainage shaft	2.0 × 2.0	1.31	1.32	5.51	Free-surface flow
No. 1 drainage shaft	2.6 × 2.6	0.43	0.47	4.97	Free-surface flow
No. 2 drainage shaft	2.6 × 2.6	0.27	0.29	3.55	Free-surface flow

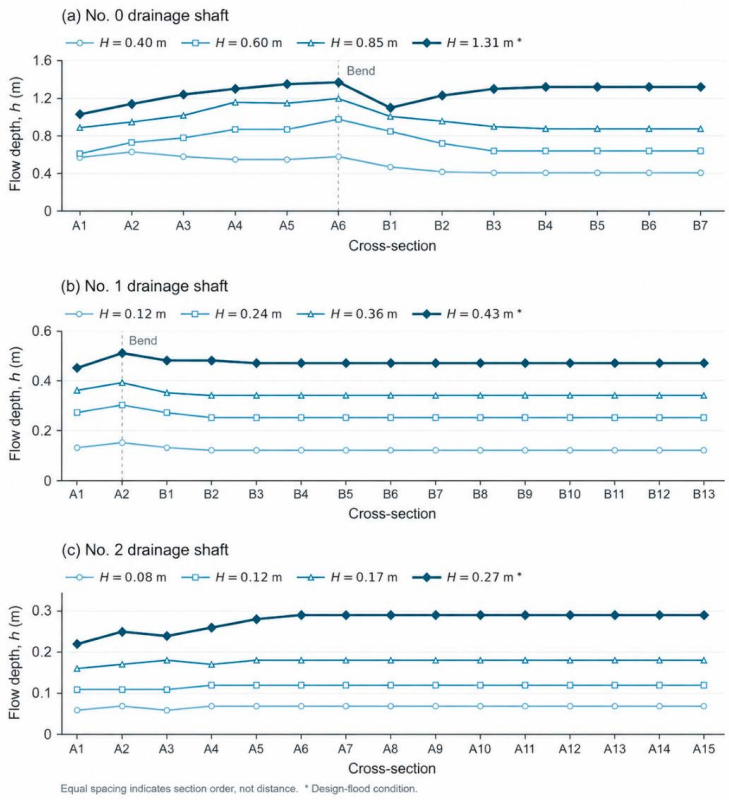


Figure 4. Longitudinal distributions of flow depth in the internal drainage tunnels under different upstream heads. (**a**) No. 0 drainage shaft; (**b**) No. 1 drainage shaft; and (**c**) No. 2 drainage shaft. Dashed vertical lines in (**a**,**b**) indicate the tunnel bends. Cross-sections are plotted at equal spacing according to their sequence rather than actual longitudinal distance. An asterisk denotes the design-flood condition.

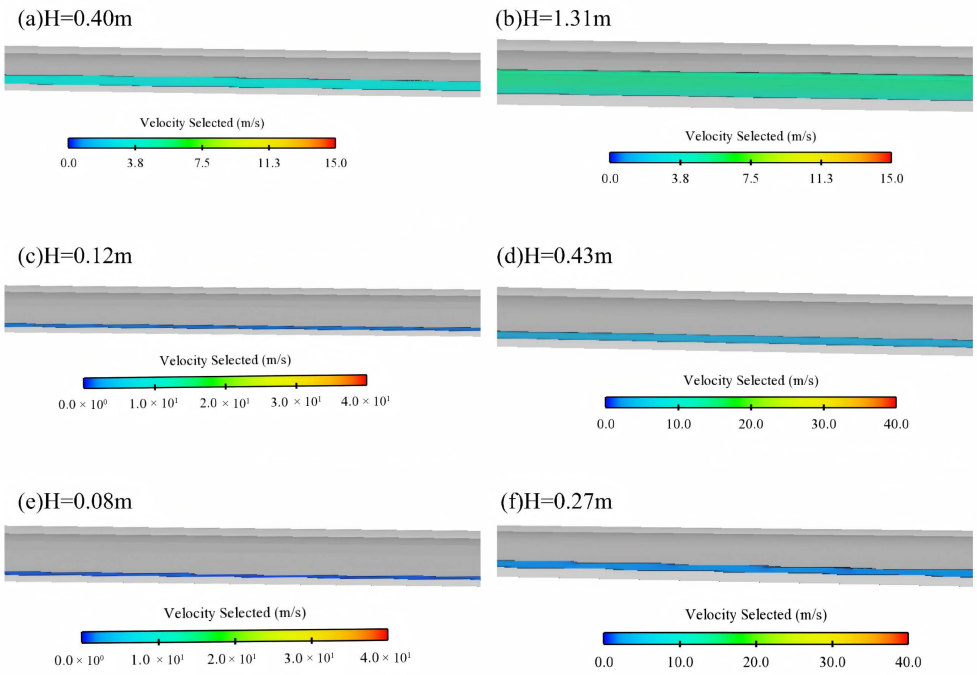


Figure 5. Longitudinal velocity fields in the internal drainage tunnels under low-head and design-flood conditions: (**a**,**b**) No. 0 drainage shaft; (**c**,**d**) No. 1 drainage shaft; and (**e**,**f**) No. 2 drainage shaft. The right-hand panels correspond to the design-flood conditions.

3.2.2. Flow-Regime Transition and Backwater Propagation in the External Cascade System

The external overflow system exhibited different hydraulic responses depending on downstream hydraulic constraints. The No. 1 and No. 2 overflow shafts were hydraulically connected through the cascade tunnels, whereas the No. 3 overflow shaft operated independently. At an upstream head of H = 1.0 m, the No. 1 and No. 2 shafts maintained free-falling nappes and the connecting tunnels remained partially filled with free-surface flow (Figure 6a,c). With increasing head, the water level within the coupled system gradually increased. At the design-flood conditions, the free-falling nappes disappeared and the connected tunnels became pressurized (Figure 6b,d). The available CFD cases bracket the transition between H = 1.0 and 2.0 m. This range is treated here as a simulated transition bracket rather than a unique critical head, because no intermediate head cases were available to resolve the onset more precisely. In comparison, the independently operating No.3 overflow shaft maintained free-surface flow under both the minimum-head condition (H = 0.5 m) and the design-flood condition (H = 2.63 m), with the tunnel remaining below the crown (Figure 7).

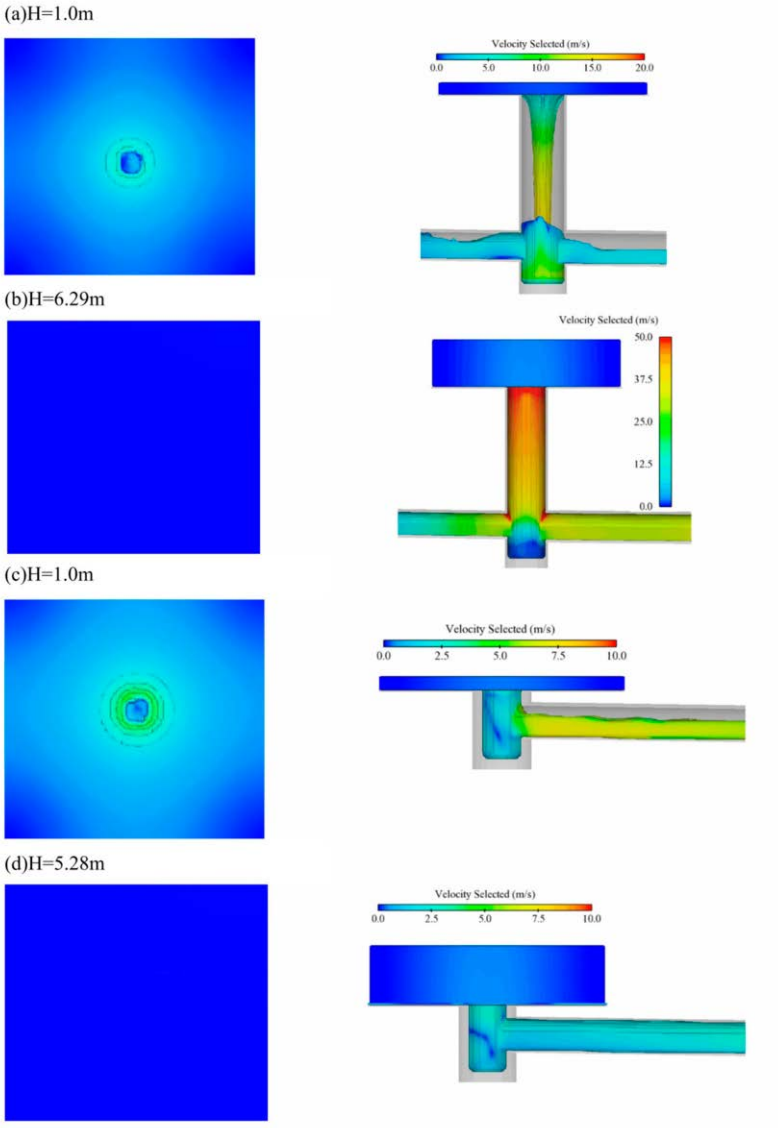


Figure 6. Flow regimes in the coupled No. 1–No. 2 overflow shaft system under different upstream heads: (**a**,**b**) No. 1 overflow shaft and (**c**,**d**) No. 2 overflow shaft. Panels (**a**,**c**) correspond to H = 1.0 m, while panels (**b**,**d**) correspond to the respective design-flood heads. Upper and lower views show the plan and longitudinal perspectives, respectively.

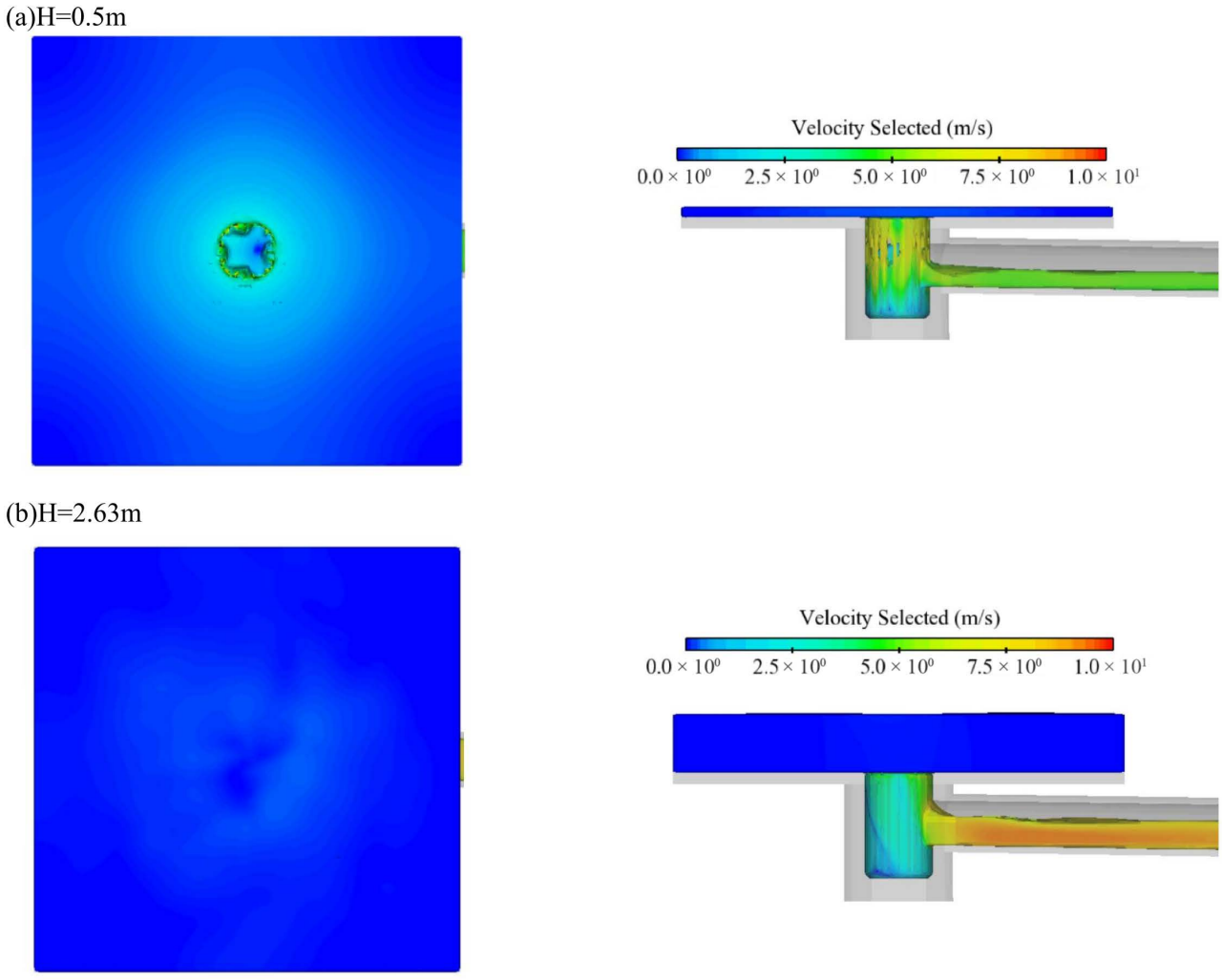


Figure 7. Flow regimes of the No. 3 overflow shaft at upstream heads of (**a**) 0.5 m and (**b**) 2.63 m.

The flow transition directly affected the discharge response of the coupled shafts. Before pressurization, discharge increased rapidly with increasing upstream head. After pressurization, the growth rate decreased, resulting in a lower slope of the H–Q curves for the No. 1 and No. 2 overflow shafts (Figure 3d,e). The discharge of the No. 1 shaft increased from 18.5 m^3/s at H = 1.0 m to 44.8 m^3/s at H = 6.29 m, while the No. 2 shaft increased from 15.8 to 33.3 m^3/s over the corresponding head range.

The longitudinal water-depth distributions clarify the mechanism responsible for the transition (Figure 8). Under high-head conditions, the downstream tunnel reach of the No.1 overflow shaft became fully occupied by water, forming a hydraulic control section near the tunnel crown. Because the discharge from the No.2 shaft subsequently entered this downstream reach, the elevated downstream water level propagated upstream and increased the backwater effect acting on the upstream structure. Consequently, the No. 2 shaft experienced a transition from free-surface to pressurized flow. The No. 3 shaft, which was isolated from downstream hydraulic interaction, showed no evidence of pressurization under the investigated conditions.

3.3. Total-Head Dissipation Characteristics and Potential Hydraulic Risks

The total-head dissipation ratios obtained for the drainage and overflow structures are summarized in Table 7. For the internal drainage shafts, η decreased gradually with increasing upstream head but remained above 90% throughout the simulated range. At the

highest simulated heads, η values were 90.8%, 93.9%, and 98.9% for the No. 0, No. 1, and No. 2 drainage shafts, respectively. The corresponding outlet velocities under design-flood conditions were 5.51, 4.97, and 3.55 m/s. The shaft with the largest vertical drop showed the lowest residual outlet velocity and the highest dissipation ratio. However, this comparison represents an engineering-scale tendency rather than a direct relationship controlled solely by shaft height.

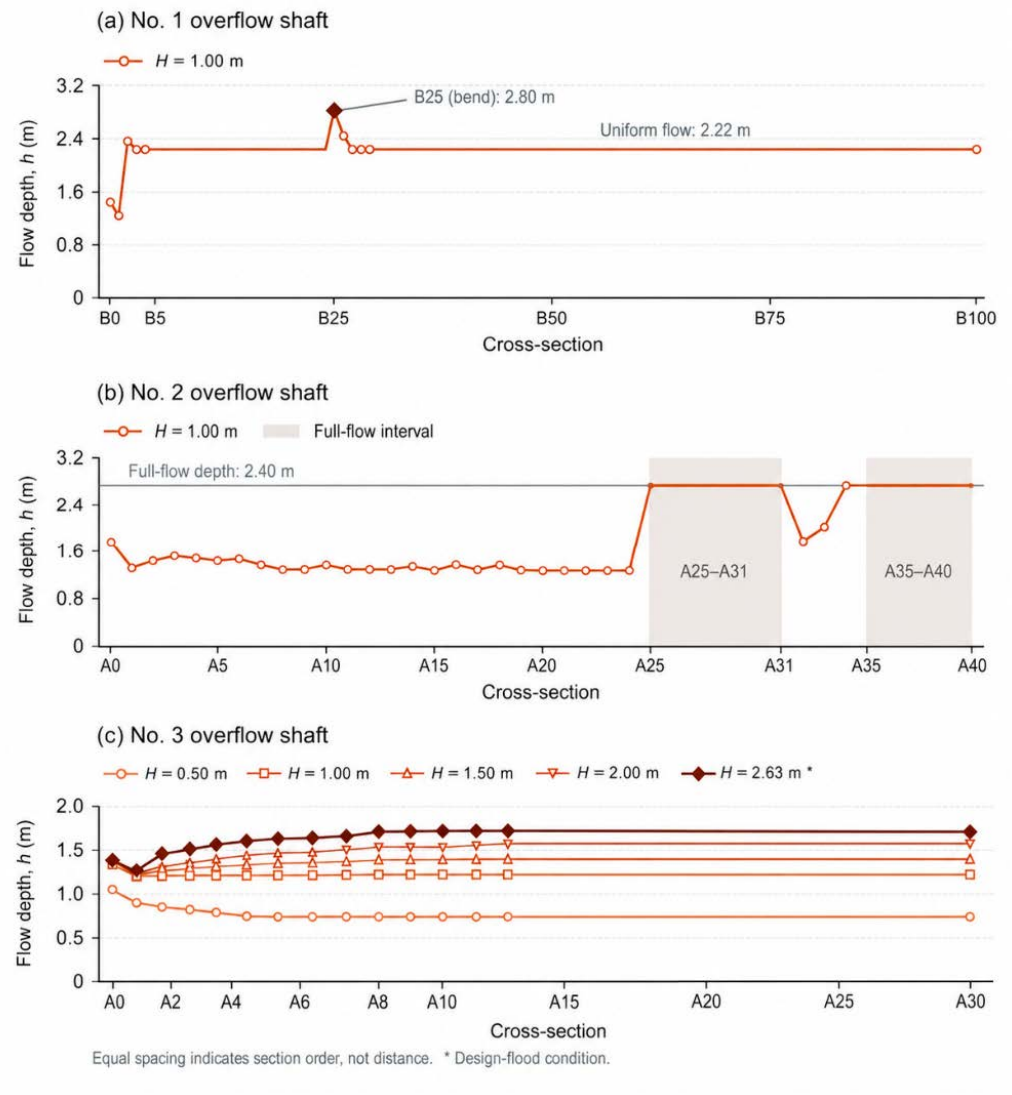


Figure 8. Longitudinal flow-depth distributions illustrating backwater propagation and flow-regime transition in the external cascade overflow tunnels. (**a**) No. 1 overflow shaft; (**b**) No. 2 overflow shaft; and (**c**) No. 3 overflow shaft. The shaded regions in (**b**) indicate full-flow intervals, and the annotated bend in (**a**) marks the local backwater rise near section B25. An asterisk denotes the design-flood condition.

Compared with the internal drainage shafts, the external overflow shafts showed lower and more variable dissipation performance. The dissipation ratios of the No. 1 and No. 2 overflow shafts remained approximately 87%, whereas that of the independent No. 3 overflow shaft decreased from 81.2% to 58.2% as the upstream head increased from 0.50 to 2.63 m. For the No. 3 shaft, this reduction was associated with the increasing residual energy carried by the outflow rather than backwater from a hydraulically connected downstream structure. A comparison at the respective highest simulated heads is shown in Figure 9.

Table 7. Total-head dissipation ratios of the flood discharge structures under the simulated conditions.

Structure	Head Over the Crest, H (m)	Inlet Total Head, E_1 (m)	Outlet Total Head, E_2 (m)	Total-Head Dissipation Ratio, η (%)
No.0 drainage shaft	0.20	30.13	0.33	98.9
	0.40	29.99	1.23	95.9
	0.60	29.96	1.91	93.6
	0.85	29.97	2.53	91.6
	1.31	31.29	2.87	90.8
No.1 drainage shaft	0.12	28.5	0.39	98.6
	0.24	28.49	0.9	96.8
	0.36	28.52	1.24	95.6
	0.43	28.49	1.73	93.9
No. 2 drainage shaft	0.08	86	0.22	99.7
	0.12	86	0.39	99.5
	0.17	85.99	0.61	99.2
	0.27	86.04	0.93	98.9
No. 1 overflow shaft	1.00	34.78	4.23	87.8
	6.29	37.85	4.75	87.4
No. 2 overflow shaft	1.00	34.78	4.23	87.8
	5.28	36.85	4.75	87.1
No. 3 overflow shaft	0.50	11.99	2.25	81.2
	1.00	11.99	4.28	64.3
	1.50	12.38	4.46	64.0
	2.00	12.77	4.69	63.3
	2.63	11.7	4.89	58.2

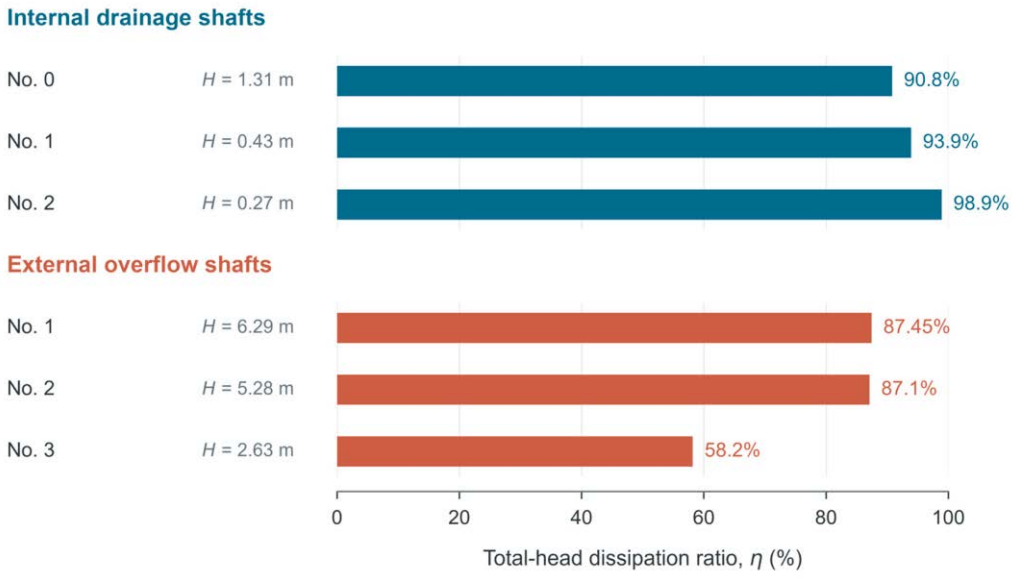


Figure 9. Comparison of total-head dissipation ratios between the internal drainage and external overflow shafts at their respective highest simulated heads.

The No. 2 drainage shaft exhibited the most pronounced localized hydraulic disturbance near the shaft bottom, where the flow underwent a 35.5 m vertical drop before entering the dissipation region. Under the design-flood condition, the downstream tunnel had a cross-sectional mean velocity of 3.55 m/s, while the total-head dissipation ratio reached 98.9% at the highest simulated head. These results indicate that most of the upstream hydraulic energy was dissipated within the shaft–tunnel system, although the dissipation process was locally concentrated near the shaft bottom. The velocity field therefore identifies this region as the principal location of concentrated hydraulic loading in the No. 2 drainage system. Because the present results describe the overall hydraulic response rather than local material damage, this region is regarded as a location requiring further

erosion and cavitation assessment, rather than as evidence that a specific lining-resistance threshold has been exceeded.

4. Discussion

4.1. Numerical Reliability and Applicability of the Numerical Model

The three-level mesh study showed monotonic convergence for all monitored quantities. Medium-to-fine differences were 0.20–0.34%, and the fine-grid GCI values were 0.084–0.143%. The selected system-scale responses were therefore stable with further mesh refinement. A separate Manning check was carried out for the stabilized free-surface reaches of the No. 1 and No. 2 drainage systems. The calculated normal depths were 0.470 and 0.275 m, compared with CFD values of 0.47 and 0.29 m, giving relative differences of 0.05% and 5.65%. This comparison is used only to judge the hydraulic consistency of these nearly uniform reaches and not to validate the pressurized-flow transition or the complex flow near shaft bottoms.

Field measurements and dedicated physical-model data were not available for the Diyan cascade. The model is regarded here as numerically verified for the system-scale responses examined, rather than independently validated for the complete cascade configuration. This distinction follows the usual separation between numerical verification and physical validation in CFD studies [26,27]. Previous FLOW-3D and related experimental–numerical studies on flood discharge shafts, vortex shafts, and free-surface hydraulic flows [9,10,13,29] are used only as supporting evidence for the applicability of the numerical framework.

RNG k-ε was used because the flow field contains strong curvature, separation, and intense mixing near the shaft inlets and bottom dissipation regions. Wall functions were applied for near-wall treatment, while y^+ distributions were not separately extracted during post-processing. The present grid-convergence results describe the stability of the monitored system-scale quantities, not the adequacy of near-wall resolution. No turbulence-closure sensitivity test was performed. Local peak velocity, pressure, and turbulence quantities near the shaft bottom are therefore treated qualitatively, while the main interpretation relies on discharge, water depth, backwater propagation, flow-regime change, and total-head dissipation.

4.2. Hydraulic Coupling Mechanism and Backwater-Induced Flow Transition

Hydraulic interaction in the external overflow system was confined to the connected No. 1–No. 2 system. The independent No. 3 shaft retained free-surface conveyance throughout the investigated conditions. The hydraulic response of the No. 1 and No. 2 shafts changed as discharge increased. At an upstream head of 1.0 m, both shafts maintained free-falling nappes and the connecting tunnels remained partially filled. Higher heads raised the downstream water level and progressively reduced the available free-surface flow area.

Flow released from the No. 2 shaft enters the downstream No. 1 system and combines with the local inflow at the lower structure. As the combined discharge increased, the downstream tunnel approached full-flow conditions. The associated rise in water level was no longer confined to the lower reach. Backwater extended upstream through the connecting tunnel, weakened the free-falling condition in the No. 2 shaft, and eventually altered the mode of conveyance. The transition therefore depended on the hydraulic state of the shared downstream reach as well as the local head acting on each shaft.

Free-surface to pressurized transitions and upstream propagation of hydraulic disturbances have also been reported in tunnel conveyance systems [14–18,30]. The geometries and boundary conditions considered in those studies differ from the present system, but

the underlying response to downstream control is comparable. In the Diyan system, the three-dimensional results show how this behaviour develops when two overflow structures share the same downstream conveyance path.

The relative differences between the simulated and design discharges also varied among the external structures. Under the design-flood condition, the relative differences were 11.4% for the independent No. 3 overflow shaft, 8.5% for the No. 2 shaft, and 2.3% for the No. 1 shaft. These values should not be interpreted as a direct positional trend because the structures differ in geometry, prescribed head, and local operating conditions. The relatively small difference at the No. 1 shaft occurred together with the strongest downstream hydraulic constraint observed in the coupled system. This result shows why the discharge capacity of a connected overflow structure cannot always be judged from its local rating relationship alone.

Within the available CFD cases, the change from free-surface to pressurized behaviour was bracketed between upstream heads of 1.0 and 2.0 m. The present head spacing does not resolve a unique critical head within this range. Finer head increments would be required to identify the onset more precisely. What is resolved by the current simulations is the hydraulic sequence leading to the transition: downstream water-level rise, upstream backwater propagation, and the subsequent change in the flow regime of the connected shaft.

4.3. Shaft Height, Energy Dissipation, and Engineering Risk

Energy dissipation in drainage shafts results from the combined effects of jet impact, turbulent mixing, and downstream energy losses rather than occurring at a single dominant location. Previous studies on vortex and drop shafts have shown that energy reduction is distributed among the inlet region, vertical shaft, and downstream dissipation zone [10,11,31,32]. Recent investigations on modified shaft geometries, such as the baffle-drop shaft with two wet sides proposed by Chen et al. [33], further indicate that localized energy dissipation patterns and residual outlet velocities can vary significantly with structural details, emphasizing the need for case-specific assessments of shaft-bottom hydraulic loading.

In this study, the three internal drainage shafts exhibited different combinations of residual outlet velocity and total-head dissipation. Under the design-flood condition, the mean outlet velocities of the No. 0, No. 1, and No. 2 drainage shafts were 5.51, 4.97, and 3.55 m/s, respectively, while the corresponding total-head dissipation ratios at the highest simulated heads were 90.8%, 93.9%, and 98.9%. The No. 2 drainage shaft, which had the largest vertical drop, showed the lowest residual outlet velocity and highest dissipation ratio. However, the three shafts differed in discharge, upstream head, and geometry; therefore, the observed trend should be considered a configuration-dependent tendency rather than a universal relationship between shaft height and energy dissipation. The lower dissipation efficiency of the independent No. 3 overflow shaft at higher heads was primarily associated with increased residual outlet energy, whereas the hydraulic response of the No. 1–No. 2 system was additionally influenced by interaction within the shared downstream conveyance path.

High overall energy dissipation does not necessarily imply mild local hydraulic conditions. In the No. 2 drainage shaft, the 35.5 m vertical drop produced pronounced impact and turbulent mixing near the shaft bottom, consistent with observations reported for other high-head shaft systems [9,11,31–33]. Although this shaft showed the highest overall dissipation efficiency, hydraulic loading remained locally concentrated near the bottom. This region should therefore be regarded as a location requiring further erosion- and cavitation-resistance assessment rather than as direct evidence of structural damage.

4.4. Limitations and Design Implications

The simulations represent independent quasi-steady hydraulic states under prescribed upstream heads rather than the transient filling process. The 1.0–2.0 m transition range should therefore be interpreted as a quasi-steady bracket rather than a unique critical head. Tru-VOF was used to track the water free surface. No separate compressible-air model was activated, and air compression, entrainment, and venting were not solved explicitly. Transient air–water interactions and pressure surges were therefore outside the scope of the present analysis [16,18,30,34]. Sediment-laden flow, long-term abrasion, and material deterioration were outside the scope of the present simulations. Recent mesoscopic damage studies based on computed tomography have shown that material degradation under repeated external disturbances can evolve progressively [35], suggesting that future work should couple localized hydraulic loading with structural and material-damage assessment.

These limitations do not alter the observed hydraulic coupling within the investigated quasi-steady conditions, but they restrict interpretation of the transition as a fully transient process. For cascade overflow systems, the hydraulic response of individual shafts should therefore be assessed together with the conveyance capacity of the connecting tunnels and the interaction among structures. For high-head drainage shafts, residual outlet energy should also be considered together with localized hydraulic loading near the shaft bottom. Three-dimensional CFD complements conventional hydraulic methods by resolving backwater propagation, free-surface–pressurized transitions, and localized flow features that are difficult to represent using one-dimensional approaches, while empirical methods remain useful for preliminary design [36].

5. Conclusions

A three-dimensional CFD model was used to investigate the hydraulic behaviour of a large tailings storage facility with interconnected flood discharge structures. The main conclusions are as follows:

1. The simulated discharges exceeded the corresponding engineering design values by 2.3–26.5%. In the external cascade system, the relative difference decreased from 11.4% for the independently operating No. 3 shaft to 8.5% for No. 2 and 2.3% for No. 1, where the strongest downstream hydraulic constraint was observed.
2. The internal drainage-shaft subsystem maintained free-surface flow throughout the simulated conditions. Hydraulic effects generated near the shaft-bottom dissipation regions remained localized and did not significantly influence upstream inlet conditions, indicating limited sensitivity of the independent drainage shafts to downstream hydraulic constraints.
3. The coupled No. 1–No. 2 external overflow system changed from free-surface to pressurized flow as the upstream head increased. The available CFD cases bracket this transition between 1.0 and 2.0 m, but do not resolve a unique critical head. The results indicate that the transition is associated with downstream hydraulic control and upstream backwater propagation rather than with the local head of an individual shaft alone.
4. The three drainage shafts showed distinct energy dissipation characteristics. The No. 2 shaft exhibited the lowest residual outlet velocity and the highest total-head dissipation ratio, although the observed tendency was affected by differences in geometry, discharge, and upstream conditions. Its localized shaft-bottom disturbance further shows that high overall dissipation does not necessarily imply low local hydraulic loading.
5. Individual structures in cascade flood discharge systems should not be assessed independently when hydraulic coupling exists between connected tunnels and shafts.

Three-dimensional CFD complements conventional hydraulic calculations by resolving flow transitions, backwater propagation, and localized high-velocity regions that are difficult to characterize using simplified approaches.

Supplementary Materials: The following supporting information can be downloaded at: https://www.mdpi.com/article/10.3390/w18192384/s1, Table S1. Complete head-discharge data for the internal drainage and external overflow structures. Table S2. Comparison of simulated and engineering design discharges under the design-flood conditions. Table S3. Reported inlet and outlet total heads and total-head dissipation ratios. Table S4. Reported numerical-model information. Table S5. Computational resources used for one production-mesh simulation of the coupled domain.

Author Contributions: H.X. conceived the study. H.X. and S.Z. designed the numerical model. X.L. and S.Y. carried out the numerical simulations. Z.C. and Y.B. processed and analyzed the simulation data. X.L. wrote the original draft of the manuscript. S.Z. and H.X. reviewed and edited the manuscript. All authors have read and agreed to the published version of the manuscript.

Funding: This research received no external funding.

Data Availability Statement: The tabulated H–Q and total-head data supporting the findings of this study are provided in the Supplementary Materials. Raw simulation files and geometric model files in this study are available on request from the corresponding author due to engineering-confidentiality restrictions.

Conflicts of Interest: The authors declare no conflicts of interest.

References

1. International Commission on Large Dams (ICOLD). *Tailings Dams: Risk of Dangerous Occurrences: Lessons Learnt from Practical Experiences*; Bulletin 121; ICOLD: Paris, France, 2001; 144p.
2. Armstrong, M.; Petter, R.; Petter, C. Why Have So Many Tailings Dams Failed in Recent Years? Resour. *Policy* **2019**, *63*, 101412. [CrossRef]
3. Rico, M.; Benito, G.; Salgueiro, A.R.; Díez-Herrero, A.; Pereira, H.G. Reported Tailings Dam Failures: A Review of the European Incidents in the Worldwide Context. *J. Hazard. Mater.* **2008**, *152*, 846–852. [CrossRef] [PubMed]
4. Piciullo, L.; Storrøsten, E.B.; Liu, Z.; Nadim, F.; Lacasse, S. A New Look at the Statistics of Tailings Dam Failures. *Eng. Geol.* **2022**, *303*, 106657. [CrossRef]
5. Rana, N.M. Global Study of Tailings Dam Failures by Statistical and Remote Sensing Methods. Ph.D. Thesis, University of Waterloo, Waterloo, ON, Canada, 2023.
6. Ghahramani, N.; Adria, D.A.M.; Rana, N.M.; Llano-Serna, M.; McDougall, S.; Evans, S.G.; Take, W.A. Analysis of Uncertainty and Sensitivity in Tailings Dam Breach-Runout Numerical Modelling. *Mine Water Environ.* **2024**, *43*, 87–103. [CrossRef] [PubMed]
7. Wang, J.; Chi, Y.; Zhang, S.; Shi, B.; Zhang, L.; Du, C.; Li, X.; Li, B.; Yang, L.; Huang, L.; et al. Quantitative Attribution of Seasonal Runoff Variations in the Yellow River Basin under Unsteady Conditions Using a Modified Budyko Framework. *J. Hydrol.* **2026**, *675*, 135588. [CrossRef]
8. Wang, J.; Zhang, S.; Chi, Y.; Shi, B.; Li, X.; Li, B.; He, P. Divergent Hydrological Responses of Multi-Depth Soil Moisture Variability to Multiple Factors on the Loess Plateau. *J. Hydrol.* **2026**, *670*, 135226. [CrossRef]
9. Liu, X.; Wang, G.; Zhao, B.; Liu, G.; Sang, Y. Discharge Capacity of the Flood Discharge Shaft in a Tailings Reservoir: An Experimental and Numerical Study. *Water* **2025**, *17*, 606. [CrossRef]
10. Zhang, W.; Wang, J.; Zhou, C.; Dong, Z.; Zhou, Z. Numerical Simulation of Hydraulic Characteristics in a Vortex Drop Shaft. *Water* **2018**, *10*, 1393. [CrossRef]
11. Crispino, G.; Contestabile, P.; Vicinanza, D.; Gisonni, C. Energy Head Dissipation and Flow Pressures in Vortex Drop Shafts. *Water* **2021**, *13*, 165. [CrossRef]
12. Zhang, C.; Zhang, L.; Zhang, S.; Cheng, J.; Wang, Z. Hydraulic Analysis of Advanced Spillway Systems in Tailings Dams under Extreme Weather Conditions. *Alex. Eng. J.* **2024**, *109*, 102–111. [CrossRef]
13. Bayon, A.; Valero, D.; García-Bartual, R.; Vallés-Morán, F.; López-Jiménez, P.A. Performance Assessment of OpenFOAM and FLOW-3D in the Numerical Modeling of a Low Reynolds Number Hydraulic Jump. *Environ. Model. Softw.* **2016**, *80*, 322–335. [CrossRef]
14. Zhou, J.; Li, Y. Modeling of the Free-Surface-Pressurized Flow of a Hydropower System with a Flat Ceiling Tail Tunnel. *Water* **2020**, *12*, 699. [CrossRef]

15. Huang, Y.; Guan, G.; Wang, K.; Mao, Z.; Yang, Z. Hybridizing FDM and FVM Scheme of High-Precision Interface Fast Capture for Mixed Free-Surface–Pressurized Flow in Large Cascade Water Delivery System. *J. Hydraul. Res.* **2023**, *61*, 502–516. [CrossRef]
16. Wang, Y.; Yu, X.; Qin, H.X.; Cheng, N.; Yu, C. Analysis of Pressure Surges for Water Filling in Deep Stormwater Storage Tunnels with Entrapped Air-Pocket Using a VOF Model. *AQUA—Water Infrastruct. Ecosyst. Soc.* **2022**, *71*, 992–1001. [CrossRef]
17. Zhang, J.M.; Xiang, S.; Tang, R.C.; Wang, Q.; Ju, X.M. Calculations and Experiments on Free-Surface–Pressurized Flow in Rectangular Water Conveyance Tunnel with Arch Crown. *J. Chang. River Sci. Res. Inst.* **2023**, *40*, 107–113. [CrossRef]
18. Zhang, X.; Liu, W.; Liu, J.; Zhang, L. Water–Air Interactions in Channel-Tunnel Water Conveyance Systems with Different Inflow Conditions. *Phys. Fluids* **2026**, *38*, 013310. [CrossRef]
19. Flow Science, Inc. *FLOW-3D, Version 11.2*; User Manual; Flow Science, Inc.: Santa Fe, NM, USA, 2016.
20. Yakhot, V.; Orszag, S.A. Renormalization Group Analysis of Turbulence. I. Basic Theory. *J. Sci. Comput.* **1986**, *1*, 3–51. [CrossRef]
21. Launder, B.E.; Spalding, D.B. The Numerical Computation of Turbulent Flows. *Comput. Methods Appl. Mech. Eng.* **1974**, *3*, 269–289. [CrossRef]
22. Hirt, C.W.; Nichols, B.D. Volume of Fluid (VOF) Method for the Dynamics of Free Boundaries. *J. Comput. Phys.* **1981**, *39*, 201–225. [CrossRef]
23. Ferziger, J.H.; Perić, M.; Street, R.L. *Computational Methods for Fluid Dynamics*, 4th ed.; Springer: Cham, Switzerland, 2020. [CrossRef]
24. *GB 50863-2013*; Code for Design of Tailings Facilities. China Planning Press: Beijing, China, 2013.
25. *GB 39496-2020*; Safety Regulations for Tailings Pond. Standards Press of China: Beijing, China, 2020.
26. Stern, F.; Wilson, R.V.; Coleman, H.W.; Paterson, E.G. Comprehensive Approach to Verification and Validation of CFD Simulations—Part 1: Methodology and Procedures. *J. Fluids Eng.* **2001**, *123*, 793–802. [CrossRef]
27. Oberkampf, W.L.; Trucano, T.G. Verification and Validation in Computational Fluid Dynamics. *Prog. Aerosp. Sci.* **2002**, *38*, 209–272. [CrossRef]
28. Chow, V.T. *Open-Channel Hydraulics*; McGraw-Hill: New York, NY, USA, 1959.
29. Velásquez, L.; Rubio-Clemente, A.; Chica, E. Numerical and Experimental Analysis of Vortex Profiles in Gravitational Water Vortex Hydraulic Turbines. *Energies* **2024**, *17*, 3543. [CrossRef]
30. Vasconcelos, J.G.; Wright, S.J. Experimental Investigation of Surges in a Stormwater Storage Tunnel. *J. Hydraul. Eng.* **2005**, *131*, 853–861. [CrossRef]
31. Hajiahmadi, A.; Crispino, G.; Ghaeini-Hessaroeyeh, M.; Gisonni, C. Effect of the Flow Regime on the Hydraulic Features Governing the Operation of Vortex Drop Shafts with Spiral Inlets. *Water Sci. Technol.* **2022**, *86*, 1095–1107. [CrossRef] [PubMed]
32. Mahmoudi-Rad, M.; Najafzadeh, M. Experimental Evaluation of the Energy Dissipation Efficiency of the Vortex Flow Section of Drop Shafts. *Sci. Rep.* **2023**, *13*, 1679. [CrossRef] [PubMed]
33. Chen, J.; Liang, P.; Lu, Y.; Wu, T. Hydraulic Characteristics and Energy Dissipation of a New Baffle-Drop Shaft with Two Wet Sides. *Can. J. Civ. Eng.* **2025**, *52*, 1010–1021. [CrossRef]
34. Gong, J.; Zhou, M.; Deng, J.; Wei, W. Characteristics of Air Flow Driven by the Water Free Surface in a Free-Flow Spillway Tunnel. *Phys. Fluids* **2023**, *35*, 013305. [CrossRef]
35. Xue, Y.; Li, X.; Wang, L.; Liu, Y.; Cao, X.; Zhang, Y. Mesoscopic Damage Enhancement in Granite under Cyclic Liquid Nitrogen Shocks Characterized by Computed Tomography and Texture Analysis. *Int. J. Rock Mech. Min. Sci.* **2025**, *194*, 106217. [CrossRef]
36. Ogras, S.; Onen, F. Numerical Analysis of Hydraulic Characteristics of Spillways and Effectiveness of Energy Dissipation Structures. *Ain Shams Eng. J.* **2026**, *17*, 103953. [CrossRef]

Disclaimer/Publisher's Note: The statements, opinions and data contained in all publications are solely those of the individual author(s) and contributor(s) and not of MDPI and/or the editor(s). MDPI and/or the editor(s) disclaim responsibility for any injury to people or property resulting from any ideas, methods, instructions or products referred to in the content.